Non-isentropic study of a closed-circuit oscillating-water-column wave energy converter

Pierre Benreguig[a], Vicente Miguel[b], Sarah Crowley[b], Jimmy Murphy[a]

[a] *MaREI Centre, Beaufort building, University College Cork, Haubowline Road, P43C573 Ringaskiddy, Co. Cork, Ireland; marei@ucc.ie*
[b] *WavEC - Offshore Renewables, Rua Dom Jerónimo Osório, nº 11, 1º, 1400-119 Lisbon, Portugal*

Abstract

The thermodynamics of the air inside a conventional Oscillating Water Column (OWC) is commonly modelled using the isentropic relationship between pressure and density. The innovative Tupperwave device is based on the OWC concept but uses non-return valves and two extra reservoirs to rectify the flow into a smooth unidirectional air flow harnessed by a unidirectional turbine. The air, flowing in closed-circuit, experiences a temperature increase due to viscous losses across the valves and turbine along the repetitive cycles of the device's operation. In order to study this temperature increase which represents a potential issue for the device operation, a non-isentropic wave-to-wire model of the Tupperwave device is developed taking into account the irreversible thermodynamic processes. The model is based on the First Law of Thermodynamics, and accounts for viscous losses at the valves and turbine as well as solar radiation and heat transfer across the device walls and inner free-surface. The results reveal that the temperature increase in the device remains harmless for its operation. The difference between the power performance of the Tupperwave device based on the non-isentropic and isentropic models is found to be relatively small. Its performance are also compared to the corresponding conventional OWC device.

Keywords: Wave energy, Oscillating Water Column, Non-isentropic study, Tupperwave, Energy balance, Valves

Introduction

Oscillating Water Column (OWC) devices are amongst the most promising types of wave energy converters because of their relative simplicity. In the most conventional sort of OWC devices, the OWC chamber is open to the atmosphere through a self-rectifying turbine. The pressure variations in the OWC chamber create a bidirectional air flow across the turbine which is able to convert energy regardless the direction of the flow. Several types of self-rectifying turbines have been developed for OWCs with various working principles, advantages and drawbacks. An extensive review of such turbines can be found in [1]. The best performing self-rectifying turbines are the biradial and twin-rotor turbines which reach respectively about 79% and 74% efficiency [2, 3] in steady flow conditions. Self-rectifying turbines are not as efficient as conventional unidirectional air turbines which may attain peak efficiencies close to 90% in steady flow conditions. The use of a unidirectional turbine in an OWC device is possible using non-return valves to create a unidirectional flow driven by the motion of the OWC. Various OWC devices using a unidirectional turbine have been studied and different methods for rectifying the air flow were considered. Among those devices, there are for example the Masuda's navigation buoy [1] and the vented OWC from Wave Swell Energy [4]. These devices are opened to the atmosphere like in a conventional OWC, whereas other devices such as the Tupperwave device work in closed-circuit.

In the Tupperwave device, a pressure differential is built between two accumulator chambers using the motion of the water column and non-return valves, in a similar way to a hydraulic circuit. Air compressibility in the large fixed volume accumulator chambers is used to store pneumatic energy which is then released smoothly across a unidirectional turbine located between the two chambers. Wave-to-wire numerical models of the Tupperwave device and of the corresponding conventional OWC device, displayed in figure 1, were developed in [5] and [6] to assess and compare their performances. The results showed that the performance of the non-return valves is of critical importance for the Tupperwave device to compete with the conventional OWC. The thermodynamics in the devices was modelled using the linearized isentropic relationship between pressure and density in the different chambers of the device and the results were validated against model scale experimental tests.

In a conventional OWC converter the air is partly renovated once in a

wave cycle (a few seconds). This prevents the averaged inner air temperature from differing significantly from the outer air temperature. As it was shown in [7], despite non-reversible processes such as viscous losses across the turbine, the use of the linearised isentropic relationship between pressure and density provides a satisfactory approximation and simplifies the numerical modelling of conventional OWC devices. This simplifying assumption is therefore commonly used in the numerical modelling of conventional OWC devices [8, 9]. The situation is different in the Tupperwave device where the air flows in closed-circuit. The energy dissipation at the non-return valves and at the imperfectly efficient turbine is likely to increase the entropy and temperature of the inner air. The validity of the isentropic assumption for the modelling of the Tupperwave device at full scale is therefore questionable. Moreover, the increase of air temperature in the device potentially represents a risk for the device operation. This potential issue, common to all closed-circuit OWC devices, and associated with others issues related to the use of non-return valves (such as cost and reliability), discouraged many developers from taking this technology further. The present study develops for the first time a non-isentropic numerical model for a closed-circuit OWC and investigates the air temperature increase in the Tupperwave device.

In section 1 and 2, the non-isentropic models of the Tupperwave device and corresponding OWC device (figure 1) are developed, taking into account irreversible thermodynamic processes such as the energy dissipation in the turbine and the valves, the heat exchanges between the inner air and the environment, and the solar radiations. In section 3, the air temperature evolution in the different chambers and the energy flows in the Tupperwave device are analysed. Finally, isentropic and non-isentropic model results are compared in order to conclude on the reliability of the isentropic simplification.

1. Tupperwave non-isentropic model

In this section, a non-isentropic model of the Tupperwave device is developed based on the wave-to-wire model built in [6]. The thermodynamic component of the model is largely revised to account for the irreversible thermodynamic processes. The other components of the model, although quasi-identical, are also briefly described to allow this publication to be read independently from the previous one.

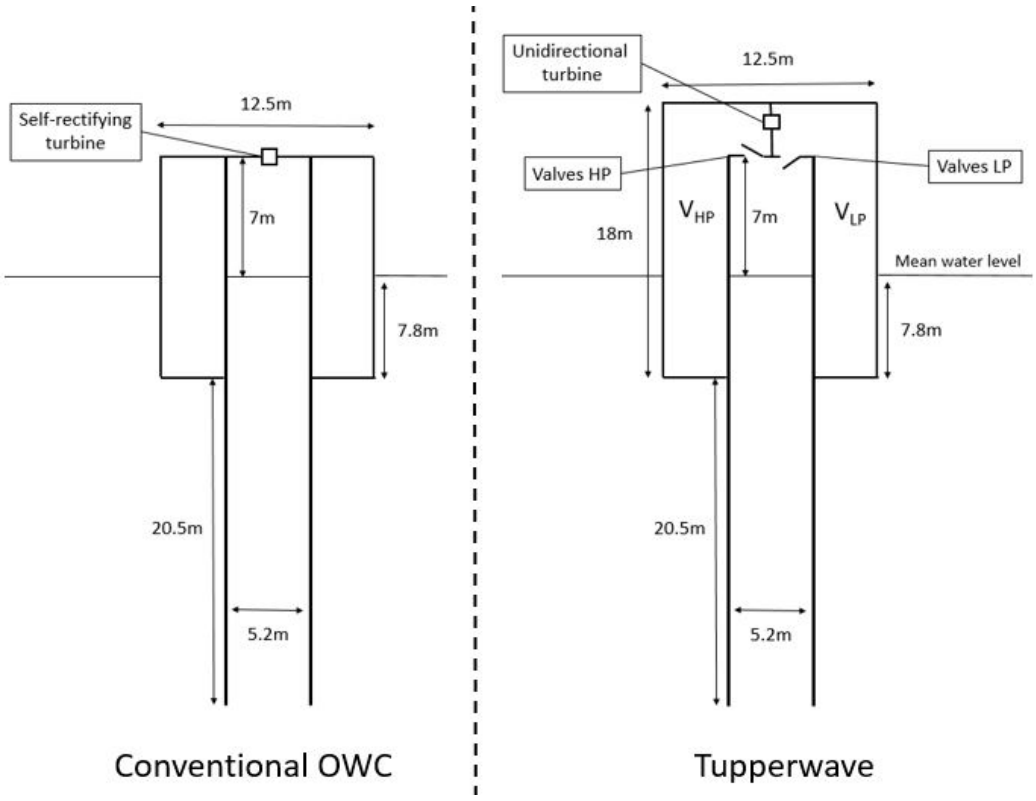

Figure 1: 2D schematic of the full scale conventional OWC and Tupperwave devices

1.1. Hydrodynamics

For the hydrodynamic modelling of the device, the two-body approach described in [10] is adopted: the first rigid body is the spar buoy structure and the second rigid body is an imaginary thin piston at the internal free surface. Both bodies are considered as rigid bodies moving only in heave due to the action of the waves. The model is based on linear wave theory. The motion of both bodies in a wave field may be modelled in the time domain applying the Cummins equation, with subscript 1 for the buoy and subscript 2 for the piston:

$$\begin{cases} [m_1 + A_{11}(\infty)]\ddot{x}_1(t) + A_{12}(\infty)\ddot{x}_2(t) + I_{11} + I_{12} + c_1 x_1(t) = f_1(t) + f_p(t) + f_{d1}(t) \\ A_{21}(\infty)\ddot{x}_1(t) + [m_2 + A_{22}(\infty)]\ddot{x}_2(t) + I_{21} + I_{22} + c_2 x_2(t) = f_2(t) - f_p(t) + f_{d2}(t) \end{cases} \tag{1}$$

where m_i are the bodies masses; c_i are the hydrostatic stiffness terms and are calculated as $c_1 = \rho_w g S_1$ and $c_2 = \rho_w g S_2$, where ρ_w is the water density, g is the acceleration of gravity, S_1 is the cross sectional area of body 1 defined by the undisturbed sea surface and S_2 is the area of the OWC free surface; $A_{ij}(\infty)$ are the bodies heaving added masses at infinite frequency (including the proper and crossed modes); f_p is the reciprocating pressure force acting on both bodies and is calculated as $f_p = S_2 p_{owc}(t)$ where p_{owc} is the excess pressure relatively to atmospheric pressure built in the OWC chamber. The terms I_{ij} are called memory effect terms and are convolution integrals:

$$I_{ij} = \int_0^t K_{ij}(t-\tau)\dot{x}_j(t)d\tau \tag{2}$$

where K_{ij} are the impulse functions for heave motions and their interactions. f_i are the wave excitation forces acting on the two bodies and are calculated as:

$$f_i(t) = \int_0^t K_{ex,i}(t-\tau)\eta(t)dt \tag{3}$$

where η is the external wave elevation and $K_{ex,i}$ is the excitation force impulse response function for body i.

The viscous drag forces f_{d1} and f_{d2} are calculated as $f_{di} = -C_{di}|\dot{x}_i(t)|\dot{x}_i(t)$, where C_{di} is the equivalent drag coefficient. The coefficients $C_{d1} = 150$ N.s^2.m^{-2} and $C_{d2} = 40$ N.s^2.m^{-2} were found in [5] to provide the best fit between the vertical displacement of the bodies predicted numerically and the ones obtained physically. For the present study, this values are converted to full scale using the Froude scaling similarity. All the hydrodynamic coefficients $A_{ij}(\infty)$, K_{ij}, $K_{ex,i}$ were computed in the frequency domain using WAMIT [11], a commercial Boundary-Element-Method software.

The volume of the OWC chamber is calculated as: $V_{owc} = V_0 + S_2(x_1 - x_2)$. The variations of V_{owc} are related to variations in p_{owc}. System of equations 1 needs to be completed by thermodynamic considerations.

1.2. Thermodynamics

In this section, the general thermodynamic equations ruling an open air chamber are derived assuming consecutively non-isentropic and isentropic assumptions. The non-isentropic model is then applied to the modelling of the Tupperwave device.

1.2.1. General equations

We consider the following open thermodynamic system: an air chamber of volume V containing a mass m of air with density $\rho = \dfrac{m}{V}$, at the temperature T and at pressure $p_{atm} + p$. w_{in} and w_{out} are the air mass flow rates, respectively, in and out of the chamber and are functions of the air excess pressure p. It is assumed that the transformations are slow enough for the thermodynamic state of air in the chamber to be uniform. The air is assumed as a perfect and dry gas of constant specific heat capacities c_v and c_p.

Non-isentropic equations. The first thermodynamic principle applied to the open system gives [9]:

$$\dot{E} = \dot{U} + \dot{E}_c + \dot{E}_p = \dot{W} + \dot{Q} + \dot{H}_{in} - \dot{H}_{out} \tag{4}$$

where E is the energy of the system; U is the internal energy; E_c and E_p are the kinetic and potential energy; $\dot{W}$ is the mechanical power provided to the system by the motion of the walls; $\dot{Q}$ is the rate of heat transfer provided to the system; $\dot{H}_{in}$ and $\dot{H}_{out}$ are the enthalpy flow rates due to exchange of matter coming in and out of the system.

The variations of the system kinetic and potential energy are neglected. Equation 4 therefore becomes:

$$\frac{d}{dt}\left(c_v m T\right) = -\left(p_{atm} + p\right)\dot{V} + \dot{Q} + c_p w_{in} T_f - c_p w_{out} T \tag{5}$$

where ρ_f and T_f are the density and temperature of the incoming air.

The Mayer's equations are:

$$\begin{cases} c_p - c_v = R & (a) \\ \frac{c_p}{c_v} = \gamma & (b) \end{cases} \tag{6}$$

where R is the specific ideal gas constant. The ideal gas law is:

$$p_{atm} + p = \rho R T \tag{7}$$

and its derivative gives:

$$\dot{p} = \dot{\rho} R T + \rho R \dot{T} \tag{8}$$

The mass balance equation gives:

$$\dot{m} = \rho \dot{V} + \dot{\rho} V = w_{in} - w_{out} \tag{9}$$

Finally, equations 5, 6.a,b, 7, 8 and 9 lead to the non-isentropic model of the system:

$$\begin{cases} \dot{m} = w_{in} - w_{out} & (a) \\ \dot{p} = \dfrac{\gamma(p_{atm}+p)}{m}\left(\dfrac{\dot{Q}}{c_p T} + w_{in}\dfrac{T_f}{T} - w_{out} - \rho\dot{V}\right) & (b) \end{cases} \tag{10}$$

System of equations 10.a,b was obtained from the 1st Thermodynamic principle and displays the general equations relating mass, density, pressure and volume of the air considered as a perfect gas in an open system during non-isentropic transformations. In this model, the specific entropy of the system is likely to change due to the irreversible processes across the valves and turbine and to the heat transferred across the boundaries of the system.

Isentropic equations. If the system is considered adiabatic and the transformations are slow enough to be reversible, the transformations become isentropic and consequently we may write:

$$\rho = \rho_{atm}\left(\frac{p_{atm}+p}{p_{atm}}\right)^{\frac{1}{\gamma}} \tag{11}$$

Equation 11 once derivated gives:

$$\dot{\rho} = \frac{\rho_{atm}\dot{p}}{\gamma p_{atm}}\left(\frac{p_{atm}+p}{p_{atm}}\right)^{\frac{1}{\gamma}-1} \tag{12}$$

Equation 12 combined with equation 9 and 11 leads to the isentropic model of the system:

$$\dot{p} = \frac{\gamma(p_{atm}+p)}{m}(w_{in} - w_{out} - \rho\dot{V}) \tag{13}$$

Equation 13 displays the equations relating mass, density, pressure and volume of the air considered as a perfect gas in an open system during isentropic transformations. Unlike in the non-isentropic system 10, the mass of air in the chamber $m = \rho V$ and the excess pressure p are directly related by the equation 11. Hence a single differential equation is necessary. We note that equation 13 can be obtained from 10.b by adding the adiabatic assumption ($\dot{Q} = 0$) and further assume no temperature difference between inner and outside air ($T_f = T$).

Linearised isentropic equations. Moreover, in the case where the excess pressure remains small compared to the atmospheric pressure, it is possible to linearise the isentropic relationship between density and pressure. Once linearised, equation 11 leads to:

$$\rho = \rho_{atm}\left(1 + \frac{p}{\gamma p_{atm}}\right) \tag{14}$$

and to:

$$\dot{\rho} = \frac{\rho_{atm}}{\gamma p_{atm}}\dot{p} \tag{15}$$

Finally, the linearised isentropic system of equations relating mass, density, pressure and volume of the system is:

$$\dot{p} = \frac{\gamma p_{atm}}{\rho_{atm} V}(w_{in} - w_{out} - \rho\dot{V}) \tag{16}$$

Depending on the feasible assumptions and on the level of accuracy desired, equations 10.a,b, or 13 or 16 can be directly applied for the modelling of the thermodynamic happening in OWC type wave energy devices air chambers. In this paper, the non-isentropic model (system of equations 10) will be used to model the thermodynamic happening in the Tupperwave device.

1.2.2. Tupperwave thermodynamics

Figure 2 displays a schematic of the 3 chambers of the Tupperwave device and their thermodynamic variables. Solid arrows represent mass flow of air and hollow arrows represent heat exchanges through the walls. Exchanges are counted positive in the direction of the arrows. Each chamber of the device is modelled as an open thermodynamic system. The non-isentropic system of equations 10.a,b is therefore applied to each of the three chambers.

In the following paragraphs, the heat transfer rates, mass flow rates and flow temperatures at the exit of the turbine and valves are mathematically expressed as functions of the temperatures and pressures in the different chambers.

Heat exchanges. In the event of air temperature increase in the device, thermal exchanges through the walls of the device need to be considered. Due to the large surface area of the walls, exchanges between the HP and LP chambers and the exterior (atmosphere and water) are considered. HP and LP chambers also exchange heat across the separation wall. Heat transfers

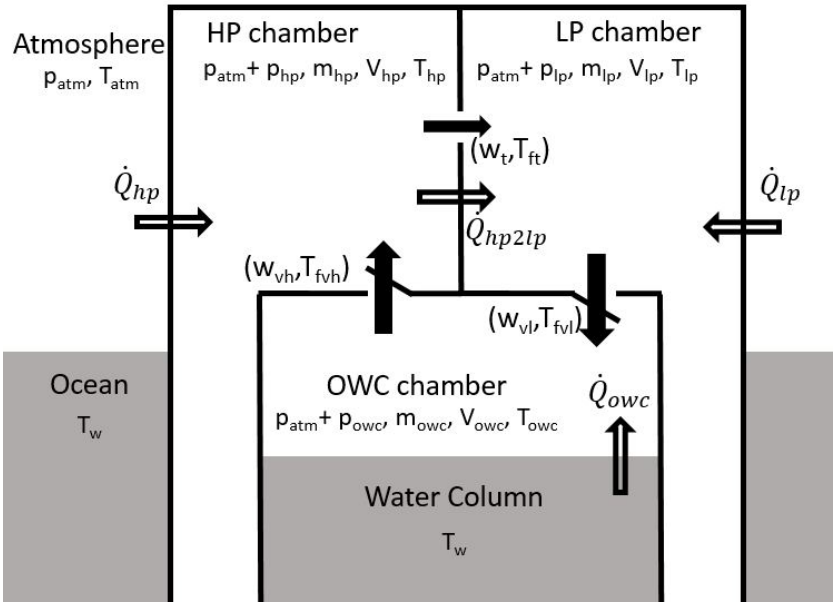

Figure 2: Tupperwave device schematic with thermodynamic variables

through the walls between the OWC chamber and the two other chambers are neglected because of the smaller common wall surface. Heat is also exchanged between the air contained in the OWC chamber and the water.

The device's walls are considered homogeneous and separate either air and water, or air and air at different temperatures. The heat transfer from a fluid 1 to a fluid 2 across a wall results of a combination in series of convection mechanisms from the fluids to the wall surfaces and conduction mechanism across the wall. To evaluate the heat transfer rate, a steady one-dimensional heat exchange model in the normal direction to the wall's surface is adopted, as displayed in figure 3. The precise study of the transient state requires to solve the unsteady heat conduction equation across the wall which would increase the mathematical complexity of the problem and was not considered by the authors. The steady state assumption will be verified in section 3 depending on the wall's material. The overall heat transfer coefficient between fluid 1 and 2 is therefore defined as [12]:

$$K_{1-2} = \frac{1}{\frac{1}{h_1} + \frac{l}{k} + \frac{1}{h_2}} \tag{17}$$

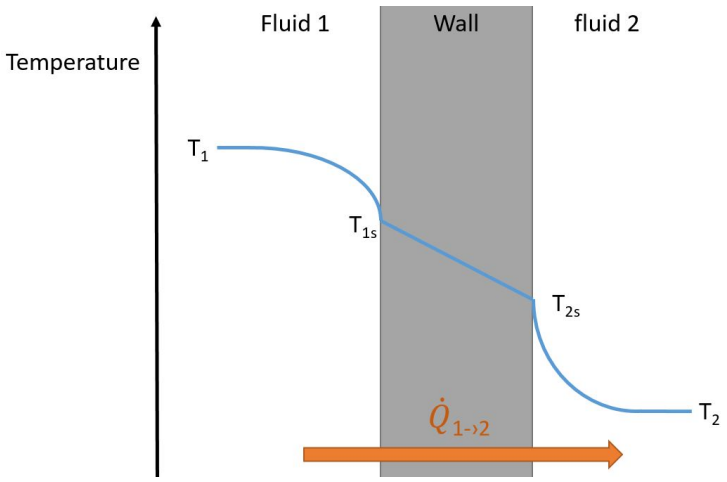

Figure 3: One-dimensional temperature evolution across a wall separating two fluids at different temperatures

where h_1 and h_2 are the fluids convective heat transfer coefficients, l and k are the thickness and heat conductivity of the wall. The heat transfer rate resulting from conduction and convection through the wall of area A, between fluid 1 at temperature T_1 and fluid 2 at temperature T_2 takes the form:

$$\dot{Q}_{1\to 2} = K_{1-2} A \left(T_1 - T_2\right) \tag{18}$$

Radiative heat transfer from the sun may play an important role in sunny days. To account for solar radiation on the device, the equivalent sol-air temperature method is used. $T_{sol-air}$ is the outside air temperature for which, in the absence of heat radiation, the external environment delivers the same heat flux to the wall surface. If the wall surface in contact with fluid 1 is exposed to sun radiation, $T_{1,sol-air}$ can be calculated as [13]:

$$T_{1,sol-air} = T_1 + \frac{\alpha I_t}{h_1} \tag{19}$$

where α the material absorptivity and I_t is the total solar irradiation. Hence, the total heat transfer rate across the wall is simply calculated as:

$$\dot{Q}_{1\to 2} = K_{1-2} A \left(T_{1,sol-air} - T_2\right) \tag{20}$$

The outside wall surface area of the HP chamber and LP chamber are approximately $A_{hp} = A_{lp} = 400\ \mathrm{m}^2$. For each chamber, about half of their

outside wall surface area is in contact with water, and the other half is in contact with air. The wall surface area of the device exposed to solar radiation is a function of the sun position and device orientation. For simplicity it is assumed that only the outside wall surface of the HP chamber in contact with air is exposed to the solar irradiation I_t. Thus, we write:

$$\dot{Q}_{hp} = K_{a-a}\frac{A_{hp}}{2}\left(T_a + \frac{\alpha I_t}{h_a} - T_{hp}\right) + K_{w-a}\frac{A_{hp}}{2}\left(T_w - T_{hp}\right) \tag{21}$$

$$\dot{Q}_{lp} = K_{a-a}\frac{A_{lp}}{2}\left(T_a - T_{lp}\right) + K_{w-a}\frac{A_{lp}}{2}\left(T_w - T_{lp}\right) \tag{22}$$

$$\dot{Q}_{hp2lp} = K_{a-a}A_{hp2lp}\left(T_{hp} - T_{lp}\right) \tag{23}$$

where the subscribes a and w respectively refer to the atmospheric air and the ocean water. Atmospheric and ocean temperatures T_a and T_w are assumed constant. $A_{hp2lp} = 135\,\mathrm{m}^2$ is the surface area of the wall separating the HP chamber from the LP chamber.

The convective heat transfer between the air in the OWC chamber and the internal water surface is calculated as:

$$\dot{Q}_{owc} = h_{aw}S\left(T_w - T_{owc}\right) \tag{24}$$

where h_{aw} is the convective heat transfer coefficient between air and water and S is the internal water surface area.

Turbine. To assess the temperature of the flow at the exit of the turbine, we consider the real expansion process happening across the turbine from the stagnation pressure $p_{0,in}$ at the inlet to the static pressure p_{out} at the outlet. The entropy-enthalpy diagram is shown in figure 4 where perfect (dashed-arrow) and real (full arrow) expansions are represented between the two isobaric lines. The kinetic energy at the entrance of the turbine is neglected and the kinetic energy in the exhaust gases is not contributing to the total useful energy at the turbine. The total-to-static efficiency of the turbine is therefore defined as:

$$\eta_t = \frac{P_m}{P_{avail}} = \frac{h_{0,in} - h_{out}}{h_{0,in} - h_{out,s}} \tag{25}$$

where P_{avail} is the available power to the turbine (defined as the power output of a perfectly efficient turbine), P_m is the power converted by the actual turbine into mechanical power, $h_{0,in}$ is the stagnation specific enthalpy at

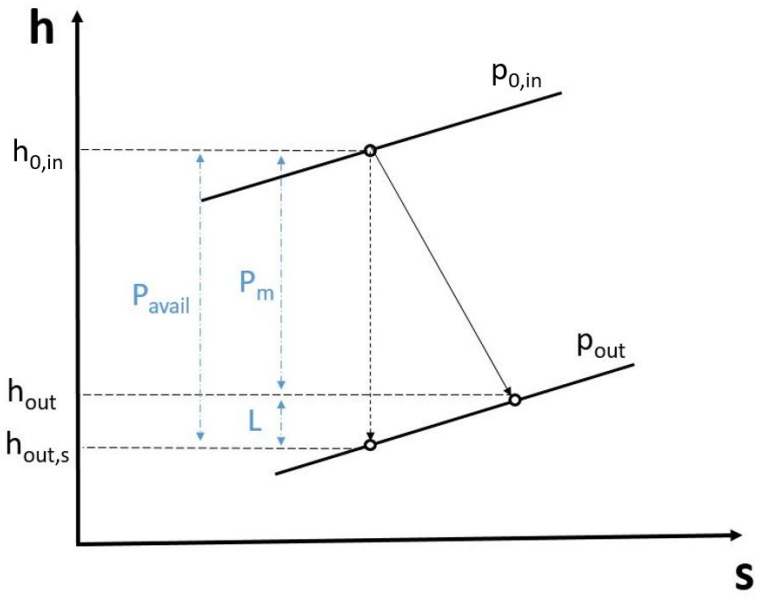

Figure 4: Specific entropy-enthalpy diagram for the turbine

the entrance of the turbine, h_{out} is the specific enthalpy at the exit of the turbine, and $h_{out,s}$ is the specific enthalpy at the exit of the turbine if the expansion were perfect (i.e. isentropic). The turbine losses are dissipated into heat and are calculated as:

$$L_t = P_{avail} - P_m = P_{avail}(1 - \eta_t) = w_{in}(h_{out} - h_{out,s}) \tag{26}$$

The air is considered as a perfect gas and so $dh = c_p dT$. Equation 26 can be written as:

$$L_t = w_{in} c_p (T_{out} - T_{out,s}) \tag{27}$$

i.e.

$$T_{out} = T_{out,s} + \frac{L_t}{c_p w_{in}} \tag{28}$$

The temperature of the flow at the exit of the isentropic expansion is calculated using the well-known isentropic relationship:

$$T_{out,s} = T_{in} \left(\frac{p_{out}}{p_{0,in}} \right)^{\frac{\gamma - 1}{\gamma}} \tag{29}$$

Applying equations 28 and 29 to the expansion from the HP to the LP chamber across the turbine leads to the expression of the air temperature at the exit of the turbine and entering the LP chamber:

$$T_{ft} = T_{hp}\left(\frac{p_{atm} + p_{lp}}{p_{atm} + p_{hp}}\right)^{\frac{\gamma-1}{\gamma}} + \frac{L_t}{c_p w_t} \tag{30}$$

The mass flow rate across the turbine now needs to be expressed. The model of the radial-inflow turbine used in this paper is taken from the literature and was obtained with a rotor of 500mm at rotational speeds between 700 and 1300rpm. The Reynolds number ranged between 9.2×10^5 and 2.1×10^6 and the Mach number did not exceed 0.1 [3]. In this conditions, the flow can be considered as incompressible. In this paper, the Tupperwave device is equipped with same turbine diameter (see table 1 in section 3) but the rotational speeds considered are 4 times higher. Changes in Reynolds and Mach number can modify the turbine performances: a higher Reynolds number may modify the turbulent behaviour of the flow and compressibility effects may be introduced if the Mach number rises above 0.3. In what follows, Mach and Reynolds number effects are ignored and the flow through the turbine is considered as approximately incompressible. Thus, the performance of the turbine can be presented non-dimensionally and the results can be applied to a geometrically similar turbine of different size, rotating at different speed and with a fluid of different density [14].

If the flow is assumed incompressible, the turbine power output P_m depends on the turbine geometry, on the turbine size (rotor diameter), on the rotational speed Ω, and on the pressure head $\Delta p_t = p_{0,in} - p_{out}$ between inlet and outlet (or on the air flow rate w_t). The corresponding dimensionless variables are the dimensionless flow coefficient Φ, dimensionless pressure head Ψ and dimensionless turbine power output Π which are defined as [1]:

$$\Phi = \frac{w_t}{\rho_{in}\Omega D^3}; \quad \Psi = \frac{\Delta p_t}{\rho_{in}\Omega^2 D^2}; \quad \Pi = \frac{P_m}{\rho_{in}\Omega^3 D^5} \tag{31}$$

Neglecting the influence of the Reynolds and Mach numbers, we may write:

$$\Psi = f_\Psi(\Phi)\ ; \quad \Pi = f_\Pi(\Phi) \tag{32}$$

where the functions f_Ψ and f_Π depend only on the turbine geometry but not on size, rotational speed or fluid density. From equations 31 and 32, the

mass flow rate through the turbine w_t and the turbine torque T_{turb} can be expressed as a functions of the pressure head and the rotational speed:

$$w_t = \rho_{hp}\Omega D^3 f_\Psi^{-1}\left(\frac{p_{0,in} - p_{out}}{\rho_{in}\Omega^2 D^2}\right) \tag{33}$$

$$T_{turb} = \frac{P_m}{\Omega} = \rho_{hp}\Omega^2 D^5 f_\Pi\left(\frac{w_t}{\rho_{in}\Omega D^3}\right) \tag{34}$$

For low Mach numbers ($M < 0.3$ as during the experimental assessment of the turbine performances [3]), the flow can be considered as incompressible and the dimensionless power available to the turbine is the product of the volumetric flow rate and the pressure head. Hence, the total-to-static turbine efficiency η_t is obtained by:

$$\eta_t = \frac{P_m}{P_{avail}} = \frac{\Pi}{\Phi\Psi} = f_\eta(\Phi) \tag{35}$$

The turbine works at maximum efficiency for the optimal dimensionless flow coefficient Φ_{opt}.

The turbine functions f_Ψ and f_Π of the unidirectional turbine used in the Tupperwave model were established at model scale during laboratory tests described in [3, 15]. This unidirectional turbine was tested in the framework of the twin-rotor turbine development which is among the most efficient self-rectifying turbine. Being symmetrical, only half of the turbine (designated single-rotor turbine) was designed, constructed and tested in unidirectional flow at Instituto Superior Tecnico (IST), Lisbon. This single-rotor turbine is used here in the Tupperwave device. It reaches 84% maximum efficiency in constant flow condition.

Valves. The non-return valves are essential for the successful performance of the Tupperwave device [5, 16]. Valves can either be passive (check valves) or active (on/off valves). The valves considered in this paper are passive valves that require a pressure head $\Delta p_v = p_{in} - p_{out}$ larger than their opening pressure p_{v0} to open. We note that each valve (HP or LP) is open only about half of the time. Therefore, the average flow rate across them when they are open is about twice as high as the average flow across the turbine. In the conditions in which the model is simulated in this paper, the Mach number of the flow across the valves sometimes rises above 0.3. Hence, the flow needs to be considered as compressible. The mass flow rates of air across the

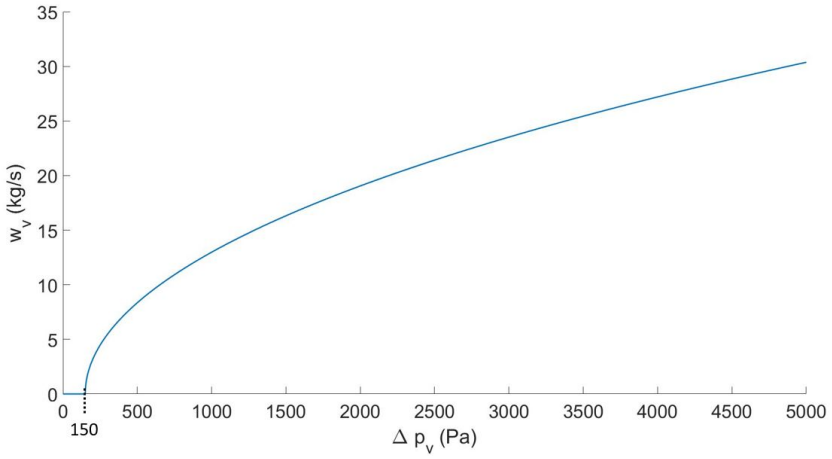

Figure 5: Mass flow rate across the valves as function of the pressure head with an opening pressure $p_{v0} = 150Pa$. For the illustration, ρ_{in} is set to atmospheric value.

valves are calculated from their pressure head using a steady-state subsonic compressible flow model [12]:

$$w_{v,in\to out} = \begin{cases} 0 & if \quad p_{in} - p_{out} < p_{v0} \\ \alpha_d A_v \sqrt{\dfrac{2\gamma}{\gamma - 1}\rho_{in}(p_{in} - p_{v0})\left(r^{\frac{2}{\gamma}} - r^{\frac{\gamma+1}{\gamma}}\right)} & if \quad p_{in} - p_{out} > p_{v0} \end{cases} \tag{36}$$

where $r = \dfrac{p_{out}}{p_{in} - p_{v0}}$ is the pressure ratio over the valve when open; A_v is the opening area of the valve; α_d is a correction coefficient called discharge coefficient, accounting for the further contraction of the flow cross-sectional area downstream of the valve opening (also called vena-contracta). As illustration, figure 5 displays the mass flow rate across the valves as function of the pressure head, for $\rho_{in} = \rho_{atm}$. In the present work, the equivalent opening area of the valves was set to $\alpha_d A_v = 0.286\,\mathrm{m}^2$ and the opening pressure set to $p_{v0} = 150$ Pa. Further considerations on the valves characteristics, although critical for the Tupperwave performances, are not in the scope of this paper.

The expansion across the valves corresponds to a throttling process and is fundamentally irreversible as the exit kinetic energy is dissipated. No work is done on or by the air and the expansion therefore happens at constant enthalpy [17]: $h_{in} = h_{out}$, i.e. for a perfect gas $T_{in} = T_{out}$. Thus, using the

ideal gas law, we have:

$$T_{fvh} = T_{owc} = \frac{(p_{atm} + p_{owc})V_{owc}}{m_{owc}R} \quad \text{and} \quad T_{fvl} = T_{lp} = \frac{(p_{atm} + p_{lp})V_{lp}}{m_{lp}R} \tag{37}$$

Finally, we have obtained the mathematical expressions of the heat transfers across the walls, the mass flow rates across the turbines and valves and their exit temperatures as functions of the pressures, volumes and masses of air in each chamber. Equations from system 10 can be directly applied to each of the three chambers of the Tupperwave device, thus obtaining the non-isentropic thermodynamic model of the device:

$$\begin{cases} \dot{m}_{owc} = w_{lp} - w_{hp} \\ \dot{m}_{hp} = w_{hp} - w_t \\ \dot{m}_{lp} = w_t - w_{lp} \\ \dot{p}_{owc} = \dfrac{\gamma(p_{atm} + p_{owc})}{m_{owc}} \left(\dfrac{\dot{Q}_{owc}}{c_p T_{owc}} + w_{vl} \dfrac{T_{lp}}{T_{owc}} - w_{vh} - \rho_{owc} \dot{V}_{owc} \right) \\ \dot{p}_{hp} = \dfrac{\gamma(p_{atm} + p_{hp})}{m_{hp}} \left(\dfrac{\dot{Q}_{hp} - \dot{Q}_{hp2lp}}{c_p T_{hp}} + w_{vh} \dfrac{T_{owc}}{T_{hp}} - w_t \right) \\ \dot{p}_{lp} = \dfrac{\gamma(p_{atm} + p_{lp})}{m_{lp}} \left(\dfrac{\dot{Q}_{lp} + \dot{Q}_{hp2lp}}{c_p T_{lp}} + w_t \dfrac{T_{ft}}{T_{lp}} - w_{vl} \right) \end{cases} \tag{38}$$

1.3. Generator model and control law

The last differential equation of the model is given by the Newton's law applied on the generator rotor:

$$I\dot{\Omega} = T_{turb} - T_{gen} \tag{39}$$

where I is the inertia of the turbine-generator system; T_{gen} is the electromagnetic braking torque of the generator and T_{turb} is given in equation 34.

A Maximum Power Point Tracking (MPPT) control strategy is applied to control the generator braking torque and optimise the instantaneous turbine efficiency. This control strategy was physically implemented in [6] on a rotary test rig to simulate the turbine-generator interaction.

The electromagnetic power $P_{em} = \Omega T_{gen}$ is finally converted into electricity by the generator with the efficiency η_{gen} which depends on its load $\Lambda = \dfrac{P_{em}}{P_{rated}}$, where P_{rated} is the generator rated power. The realistic generator efficiency is displayed in figure 6 and drops very sharply for partial loads.

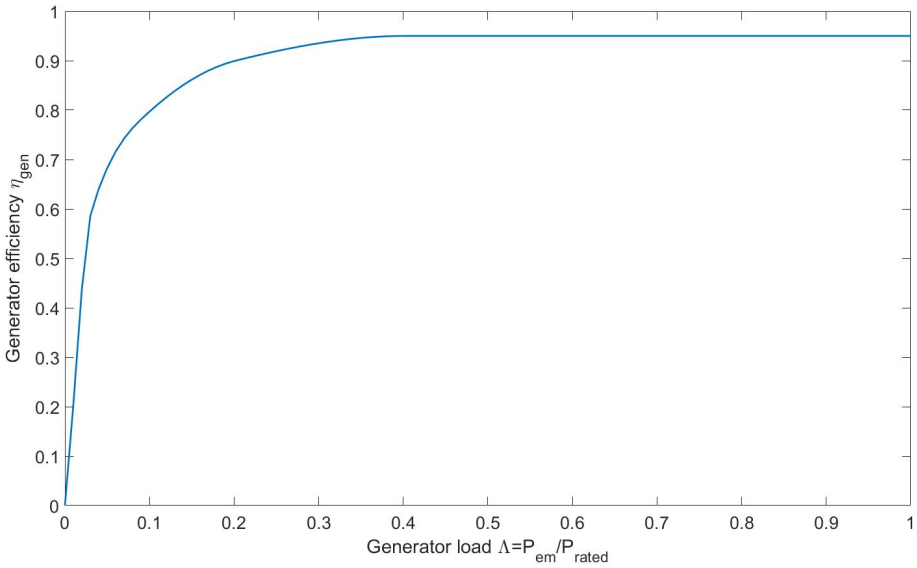

Figure 6: Generator efficiency curve as a function of the load [18]

1.4. Global numerical model and numerical integration method

The systems of differential equations 1, 38 and 39 constitute the model of the Tupperwave device. Computing the solution of these equations to find the nine unknown variable $(x_1, x_2, m_{owc}, m_{hp}, m_{lp}, p_{owc}, p_{hp}, p_{lp}, \Omega)$ is made difficult by the fact that equations from the system 1 are second-order differential equations and by the presence of the memory effect convolution integrals I_{ij}.

In the present work, the memory effect terms are approximated using a state-space representation. Each of the four convolution integrals I_{ij} can be approximated by the sum of n additional state variables $I_{ij,k}$, using the Prony's method [19, 20]:

$$I_{ij} \simeq \sum_{1}^{n} I_{ij,k} \tag{40}$$

Each $I_{ij,k}$ is governed by an additional first order differential equation of the form:

$$\dot{I}_{ij,k} = \beta_{ij,k} I_{ij,k} + \alpha_{ij,k} \dot{x}_j \tag{41}$$

Moreover the two second order differential equations of the system 1 can be reduced to first order differential equations by introducing the matrix variables $U = \begin{bmatrix} x_1 \\ x_2 \end{bmatrix}$ and $V = \begin{bmatrix} \dot{x}_1 \\ \dot{x}_2 \end{bmatrix}$.

Finally, the system of equations governing the non-isentropic wave-to-wire model of the Tupperwave device can be expressed as:

$$\begin{cases} \dot{U} = V \\ \dot{V} = M^{-1}\left(\begin{bmatrix} f_1 \\ f_2 \end{bmatrix} + \begin{bmatrix} 1 \\ -1 \end{bmatrix} Sp_{owc} - \begin{bmatrix} \sum_1^n I_{11,k} + \sum_1^n I_{12,k} \\ \sum_1^n I_{21,k} + \sum_1^n I_{22,k} \end{bmatrix} - \begin{bmatrix} C_{d1} \\ C_{d2} \end{bmatrix} .V. |V| - \begin{bmatrix} c_1 \\ c_2 \end{bmatrix} .U \right) \\ \dot{I}_{11,k} = \beta_{11,k} I_{11,k} + \alpha_{11,k} \dot{x}_1, \qquad k = 1:n \\ \dot{I}_{12,k} = \beta_{12,k} I_{12,k} + \alpha_{12,k} \dot{x}_2, \qquad k = 1:n \\ \dot{I}_{21,k} = \beta_{21,k} I_{21,k} + \alpha_{21,k} \dot{x}_1, \qquad k = 1:n \\ \dot{I}_{22,k} = \beta_{22,k} I_{22,k} + \alpha_{22,k} \dot{x}_2, \qquad k = 1:n \\ \dot{m}_{owc} = w_{lp} - w_{hp} \\ \dot{m}_{hp} = w_{hp} - w_t \\ \dot{m}_{lp} = w_t - w_{lp} \\ \dot{p}_{owc} = \dfrac{\gamma(p_{atm} + p_{owc})}{m_{owc}} \left(\dfrac{\dot{Q}_{owc}}{c_p T_{owc}} + w_{vl} \dfrac{T_{lp}}{T_{owc}} - w_{vh} - \rho_{owc} \dot{V}_{owc} \right) \\ \dot{p}_{hp} = \dfrac{\gamma(p_{atm} + p_{hp})}{m_{hp}} \left(\dfrac{\dot{Q}_{hp} - \dot{Q}_{hp2lp}}{c_p T_{hp}} + w_{vh} \dfrac{T_{owc}}{T_{hp}} - w_t \right) \\ \dot{p}_{lp} = \dfrac{\gamma(p_{atm} + p_{lp})}{m_{lp}} \left(\dfrac{\dot{Q}_{lp} + \dot{Q}_{hp2lp}}{c_p T_{lp}} + w_t \dfrac{T_{ft}}{T_{lp}} - w_{vl} \right) \\ I\dot{\Omega} = T_{turb} - T_{gen} \end{cases} \tag{42}$$

This system is composed of 9+4n first order differential equations which can be solved using a numerical first-order differential equation solver. In the present work, the order of the Prony's function is $n = 4$. The system is solved with the variable step ordinary differential equation solver ode45 from the software MATLAB.

2. Conventional OWC non-isentropic model

The wave-to-wire model of the corresponding OWC device is relatively similar to the Tupperwave device. Since both devices use the same floating spar structure, the hydrodynamic set of equations is the same. Figure 7 displays a schematic of the OWC thermodynamic system. The air in the chamber is thermally isolated from the atmosphere by the buoyancy volume around the chamber. Heat exchange however occurs by convection between

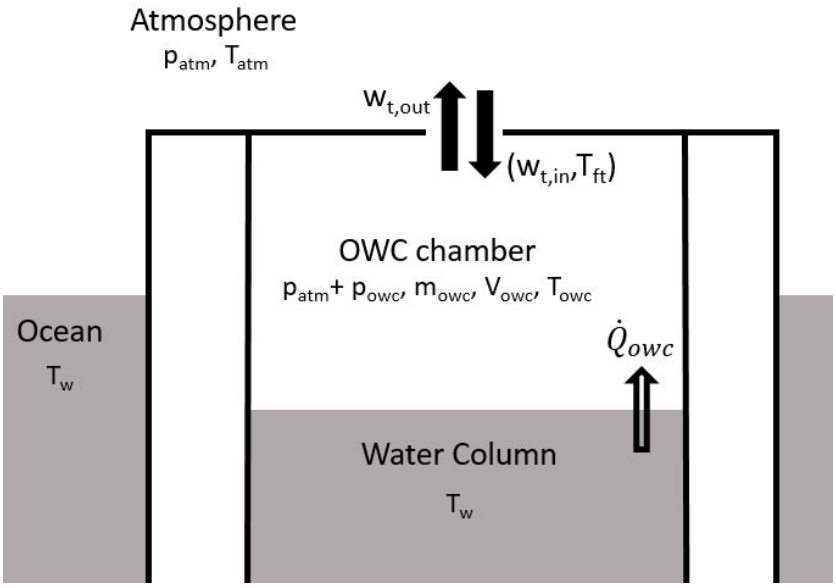

Figure 7: Conventional OWC schematic with thermodynamic variables

the air and the water column. To separate inhalation and exhalation processes, we define the two positive quantities $w_{t,in}$ and $w_{t,out}$ as the absolute values of the air flow rates respectively entering and exiting the turbine such that:

$$\text{for} \quad p_{owc} < 0 \ : \begin{cases} w_{t,in} = |w_t| \\ w_{t,out} = 0 \end{cases} \quad \text{and for} \quad p_{owc} > 0 \ : \begin{cases} w_{t,in} = 0 \\ w_{t,out} = |w_t| \end{cases} \tag{43}$$

The system of equations 10 applied on the OWC chamber gives:

$$\begin{cases} \dot{m}_{owc} = w_{t,in} - w_{t,out} \\ \dot{p}_{owc} = \dfrac{\gamma(p_{atm} + p_{owc})}{m} \left(\dfrac{\dot{Q}_{owc}}{c_p T_{owc}} + w_{t,in} \dfrac{T_f}{T_{owc}} - w_{t,out} - \rho_{owc} \dot{V}_{owc} \right) \end{cases} \tag{44}$$

with:

$$T_{ft} = T_{atm} \left(\frac{p_{atm} + p_{owc}}{p_{atm}} \right)^{\frac{\gamma-1}{\gamma}} + \frac{L}{c_p w_t} \tag{45}$$

The turbine used in the OWC model is the twin-rotor turbine. The turbine is based on a pair of conventional radial-inflow rotors mounted on

the same shaft, complemented by the corresponding guide vane rows, and by a two-position cylindrical valve which orientates the air across one rotor or the other depending on the flow direction (inhalation or exhalation). The rotor spinning in no flow generates a braking torque and causes windage losses [3]. The turbine's characteristic functions f_Ψ and f_Π were established by physical testing in [15], as well as an expression of the windage torque as a function of the rotational speed. The maximum efficiency of the twin-rotor turbine is 74% in constant flow condition.

The generator and its control law are the same as in the Tupperwave model. The only difference is that the aerodynamic friction torque T_{wind} created by the passive rotor (the one with no flow) is added in the shaft rotational speed's differential equation:

$$I\dot{\Omega} = T_{turb} - T_{gen} - T_{wind} \tag{46}$$

Using the same method as in section 1.4, the system of equations governing the non-isentropic wave-to-wire model of the conventional OWC device is expressed as 5+4n first-order differential equations:

$$\begin{cases} \dot{U} = V \\ \dot{V} = M^{-1}\left(\begin{bmatrix} f_1 \\ f_2 \end{bmatrix} + \begin{bmatrix} 1 \\ -1 \end{bmatrix} Sp_{owc} - \begin{bmatrix} \sum_1^n I_{11,k} + \sum_1^n I_{12,k} \\ \sum_1^n I_{21,k} + \sum_1^n I_{22,k} \end{bmatrix} - \begin{bmatrix} C_{d1} \\ C_{d2} \end{bmatrix} .V.|V| - \begin{bmatrix} c_1 \\ c_2 \end{bmatrix} .U \right) \\ \dot{I}_{11,k} = \beta_{11,k} I_{11,k} + \alpha_{11,k}\dot{x}_1, \qquad k = 1:n \\ \dot{I}_{12,k} = \beta_{12,k} I_{12,k} + \alpha_{ij,k}\dot{x}_2, \qquad k = 1:n \\ \dot{I}_{21,k} = \beta_{21,k} I_{21,k} + \alpha_{ij,k}\dot{x}_1, \qquad k = 1:n \\ \dot{I}_{22,k} = \beta_{22,k} I_{22,k} + \alpha_{ij,k}\dot{x}_2, \qquad k = 1:n \\ \dot{m}_{owc} = w_{t,in} - w_{t,out} \\ \dot{p}_{owc} = \dfrac{\gamma(p_{atm} + p_{owc})}{m}\left(\dfrac{\dot{Q}_{owc}}{c_p T_{owc}} + w_{t,in}\dfrac{T_f}{T_{owc}} - w_{t,out} - \rho_{owc}\dot{V}_{owc} \right) \\ I\dot{\Omega} = T_{turb} - T_{gen} - T_{wind} \end{cases} \tag{47}$$

3. Numerical results

In this section, the numerical results are obtained assuming an atmosphere and ocean temperature of 15°C. At the beginning of each simulation, the device is idle and the air in the device is at atmospheric condition.

The same turbine blade geometry as the one tested in [3] was used in both device. The diameters and rotational speeds were optimised in [6] to maximise the electrical power output from both devices in the wave climate of the EMEC test site, located in the north of Scotland. Information on the turbine and generator parameters used in the Tupperwave and the conventional OWC model are given in table 1.

Table 1: Turbine and generator parameters used in the models

		Tupperwave	**Conventional OWC**
Turbine	Type	Unidirectional radial inflow turbine	Self-rectifying radial inflow twin-rotor turbine
	Diameter (m)	0.50	1.10
	Design speed (rpm)	4000	1000
	Inertia (kg.m2)	1.7	38
	Max. efficiency (%)	86.6	73.9
Gearbox	Gearing Ratio	4	1
Generator	Rated power (kW)	100	
	Inertia (kg.m^2)	3.6	
	Design speed (rpm)	1000	
	Max. speed (rpm)	2000	
	Min. speed (rpm)	400	

As shown in table 1, the optimisation results were very different on what concerns the size (diameter D) and the rotational speed. This is due to the very different working conditions of the turbines in the two devices as can be seen in figure 8 which displays the pressure head and the flow rate to which both turbines are subjected in the same sea state. The pressure head across the Tupperwave turbine is larger with a lower flow rate. This is confirmed by the very different sizes of the orifices used to simulate the turbines in model testing of Tupperwave and conventional OWC in [5]. The higher rotational speed of the Tupperwave turbine unfortunately requires the use of a gearbox, associated with undesirable cost and maintenance issues. It can be found from the well-known Cordier diagram [21], that the use of different turbine design with a larger diameter could avoid the use of a gearbox and enable the direct driving the generator.

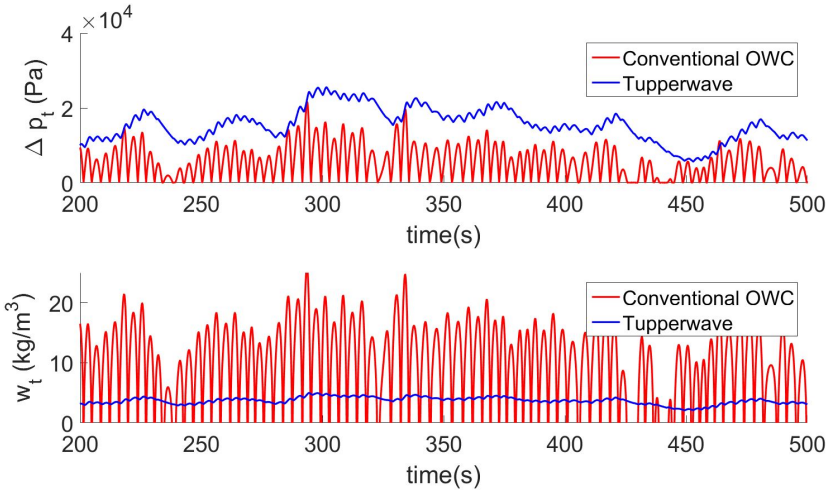

Figure 8: Pressure head and mass flow rate across the turbines in the Tupperwave device and the conventional OWC in sea state $\{H_s = 3\,\mathrm{m}\,;\, T_p = 9\,\mathrm{s}\}$

3.1. Temperature analysis

3.1.1. In the Tupperwave device

Adiabatic case. Figure 9 displays the temperature of the air in the HP and LP chambers in the case where the device does not receive any radiation from the sun and no heat exchange is allowed across the walls or with the water (adiabatic):

$$\dot{Q}_{owc} = \dot{Q}_{hp} = \dot{Q}_{lp} = \dot{Q}_{hp2lp} = 0$$

The simulation is 30-minute long in the irregular sea state $\{H_s = 3\,\mathrm{m}\,;\, T_p = 9\,\mathrm{s}\}$, which represents a relatively common sea state of moderate energy in offshore ocean conditions. The black line represents the average air temperature of the system at the end of the simulation.

Given the pressure difference between the two chambers, the HP chamber is naturally hotter than the LP chamber. The temperature in the OWC chamber oscillates successively between the temperatures of the HP and LP chambers and was not represented in the figure for clarity. Significant temperature elevation occurs in the chambers due to the viscous losses. The air temperature in both chambers increases steadily by approximately 20°C in 30 minutes and would keep rising to infinity in this theoretical case. As a result, the air expands and the average pressure in the device increases.

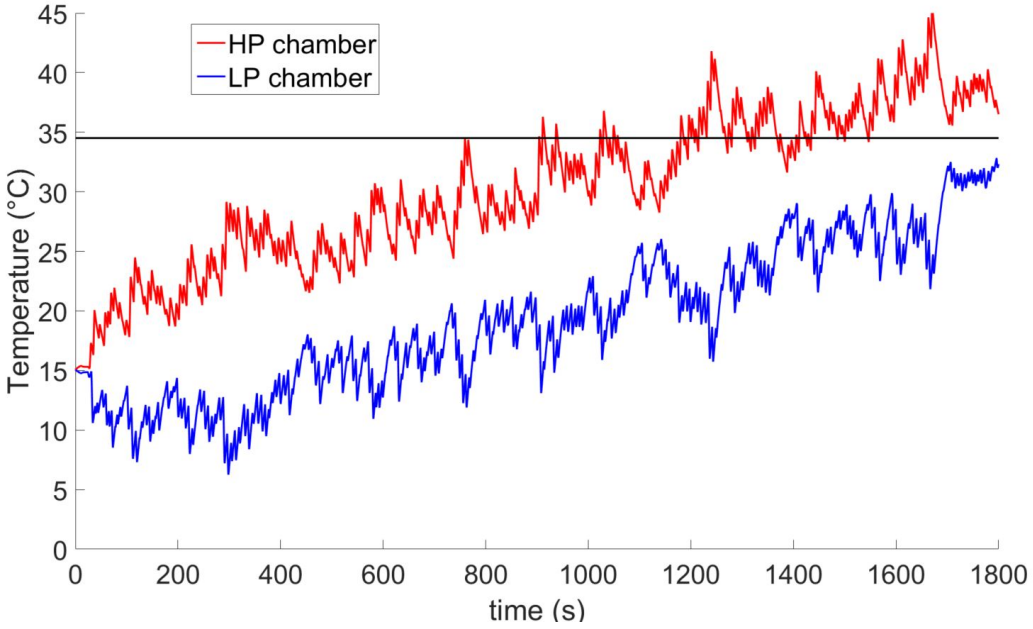

Figure 9: Air temperature in HP and LP chambers in adiabatic scenario for sea state $\{H_s = 3\,\mathrm{m}\,;\, T_p = 9\,\mathrm{s}\}$

This pushes the water column down and the buoy up and would eventually modify the hydrostatic equilibrium and the hydrodynamics of the device. High temperatures are also undesirable because they could damage on-board instrumentation or the buoy structure itself.

Diathermal case. In reality, heat transfers need to be considered due to the large outer wall's surface area of the Tupperwave device and the contact between air and water in the OWC chamber. The total solar irradiation at sea level $I_t = 1000\ \mathrm{W/m^2}$, corresponding to a clear summer day in Europe, is adopted. This value is generally used as standard test conditions for photovoltaic devices. The absorptivity α of the solar radiation by a surface is complex to assess and can vary from 0 to 1 depending on the material, the colour and the roughness of the surface. In general it is higher for dark colours and rough surface. The value $\alpha = 0.7$ is adopted for this study and corresponds to the absorptivity of concrete according to [22]. Values for the convective heat transfer coefficients between the fluids (air or water) and device walls strongly depends on the fluid properties, the roughness of the

surface and on the flow velocity in the vicinity of the wall. In the present case, the fluid flows around the device depend on the wind and water current, as well as on the motion of the device due to the wave excitation. The overall air flow velocity around the device is taken of $v_1 = 5$ m/s and the empirical law suggested in [22] leads to a convective heat transfer coefficient $h_a = 4 + 4v_1 = 24\,\mathrm{W/(m^2.K)}$. Assuming a turbulent flow of water outside the device with 1 m/s average overall speed, the convective heat transfer coefficient of the water is estimated using the Dittus-Boelter equation to $h_w = 1000\,\mathrm{W/(m^2.K)}$ [23]. Considering the motion of the IWS in the OWC chamber of approximately $v_2 = 1$ m/s, the forced convection model adopted in [24] leads to convective heat transfer coefficient between air and water $h_{aw} = 2.8 + 3v_2 = 5.8\,\mathrm{W/(m^2.K)}$. We note that the values of the thermal parameters given in this paragraph can vary largely depending on the adopted assumptions relative to the weather conditions, the device construction and the sea state. Choosing realistic values is made even more difficult by the large variability of information found in the literature. The chosen values are meant to represent the heat exchanges in light wind, current and wave conditions on a very sunny day around noon in order to avoid the underestimation of the temperature rise in the device.

The walls are first considered to be made of concrete with a thickness $l = 20$ cm. The thermal conductivity of concrete is greatly affected by mix proportioning, aggregate types and sources, as well as moisture status. Complex considerations on concrete are beyond the scope of this paper. Measurements made in [25] give an average value of $k_{th,concrete} = 2\,\mathrm{W/(m.K)}$. Figure 10 displays the temperature of the air in the HP and LP chambers in the case of a concrete buoy structure in sea state $\{H_s = 3\,\mathrm{m}\,;\, T_p = 9\,\mathrm{s}\}$. The black line represents the average air temperature in the chambers at the end of the simulation. After a transient state of about 10 minutes where the temperature increases slowly, the system reaches a steady state and the average air temperature settles 10°C higher than the initial temperature. In 5 meter high waves, the same phenomenon is observed and the increase in temperature is found to be of about 16°C.

Another wall material is considered, with a higher heat conductivity than that of concrete. The walls are assumed made of steel sheets of thickness $l = 15$ mm, and with heat conductivity $k_{th,steel} = 30\,\mathrm{W.m^{-1}.K^{-1}}$ [12]. Assuming similar walls surface colour and roughness as for the concrete walls,

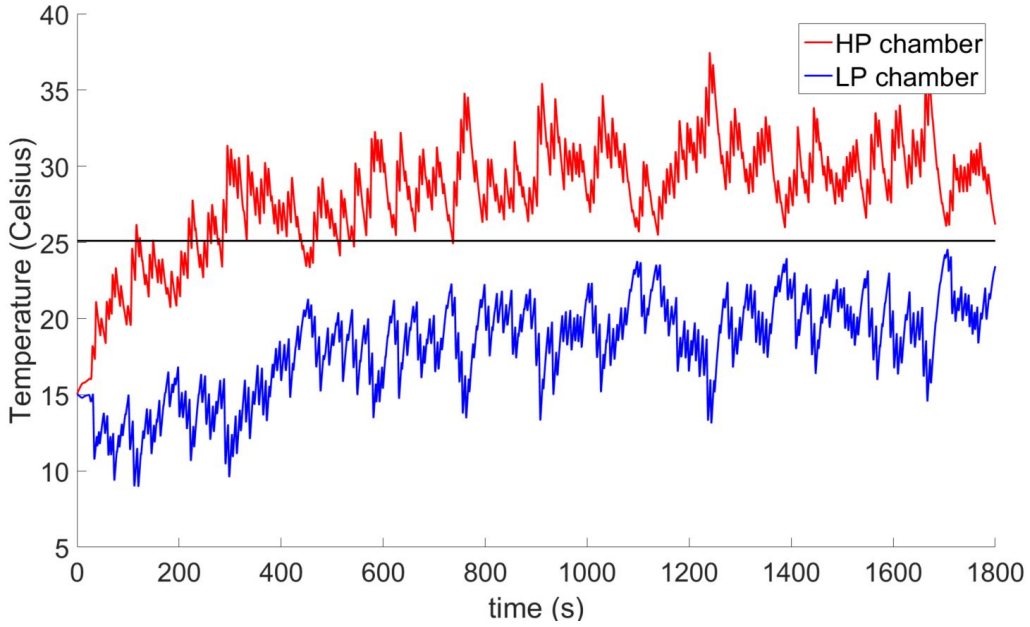

Figure 10: Air temperature in HP and LP chambers assuming heat transfers across the concrete buoy structure and with the water column for sea state $\{H_s = 3\,\mathrm{m}\,;\, T_p = 9\,\mathrm{s}\}$

the same convective heat transfer and absorptivity coefficients are adopted. Figure 11 displays the temperature of the air in the HP and LP chambers in the case of a concrete buoy structure in sea state $\{H_s = 3\,\mathrm{m}\,;\, T_p = 9\,\mathrm{s}\}$. In that case, the steady state is reached in about 5 minutes. The average air temperature increase in the device is of 6.3°C and reaches 8.5°C in extreme sea states. Simulations were also carried out in the absence of solar radiation (night conditions). The results obtained on temperature increase in the Tupperwave device under the assumption of steady state heat transfer across the walls are summarized in Table 2.

The assumption of steady state conductive heat transfer across the device walls adopted in section 1.2.2 can be checked by the calculation of the characteristic diffusion time τ across the thickness l of the wall [26]:

$$\tau = \frac{l^2}{D_{th}} = \frac{l^2 \rho c_v}{k_{th}} \tag{48}$$

where D_{th}, ρ, c_v and k_{th} are respectively the thermal diffusivity, density, heat capacity and heat conductivity of the wall material. For the steel wall, the

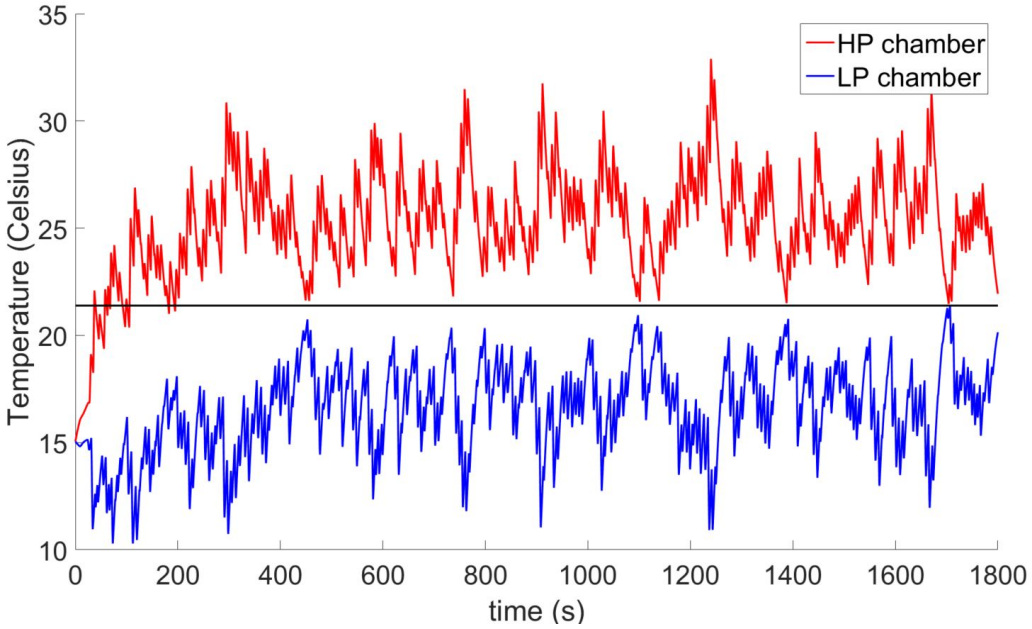

Figure 11: Air temperature in HP and LP chambers assuming heat transfers across the steel buoy structure and with the water column for sea state $\{H_s = 3\,\mathrm{m}\,;\, T_p = 9\,\mathrm{s}\}$

Table 2: Average air temperature increase from atmospheric conditions in the Tupperwave device depending the wall structure and solar irradiation and assuming steady state conductive heat transfer across the walls

Sea state	**Solar irradiation**	**Wall structure**	
		Concrete $k_{th} = 2\,\mathrm{W/(m.K)}$ $l = 20\,\mathrm{cm}$	**Steel** $k_{th} = 30\,\mathrm{W/(m.K)}$ $l = 15\,\mathrm{mm}$
$H_s = 3\,\mathrm{m}\,;\, T_p = 9\,\mathrm{s}$	$I_t = 1000\,\mathrm{W/m^2}$	10.0°C	6.3°C
	$I_t = 0\,\mathrm{W/m^2}$	4.0°C	1.5°C
$H_s = 5\,\mathrm{m}\,;\, T_p = 9\,\mathrm{s}$	$I_t = 1000\,\mathrm{W/m^2}$	15.8°C	8.5°C
	$I_t = 0\,\mathrm{W/m^2}$	9.8°C	3.7°C

characteristic diffusion time is about 30 seconds. In that case, the conductive heat transfer across the wall is quickly established and the assumption of steady state conductive heat transfer enabling a resistive thermal model of the walls is reasonable at all times. For the concrete wall, the characteristic time of diffusion is close to 10 hours. This means that, after the

sudden change of excitation force or solar radiation, the conduction heat transfer requires a 10-hour long transient state to settle back to a steady state. Hence, the resistive thermal model of the concrete wall is not valid during such transient state. The results displayed in figure 10 are therefore likely to underestimate the duration of the transient state, and higher temperature levels are likely to be reached during this period before the steady state is settled. The installation of steel heat exchangers across the concrete walls could be a solution to prevent high temperature increase caused by the sudden increase of the wave excitation force or solar radiation on the device. The temperature increase displayed in Table 2 are however still valid under the assumption that the conductive heat transfer across the walls has had sufficient time to settle. Such low air temperature increase does not represent any danger for the device operation.

The isentropic model does not predict this increase in temperature, as it can be seen in figure 12. The average air temperature in the device remains equal to the initial temperature.

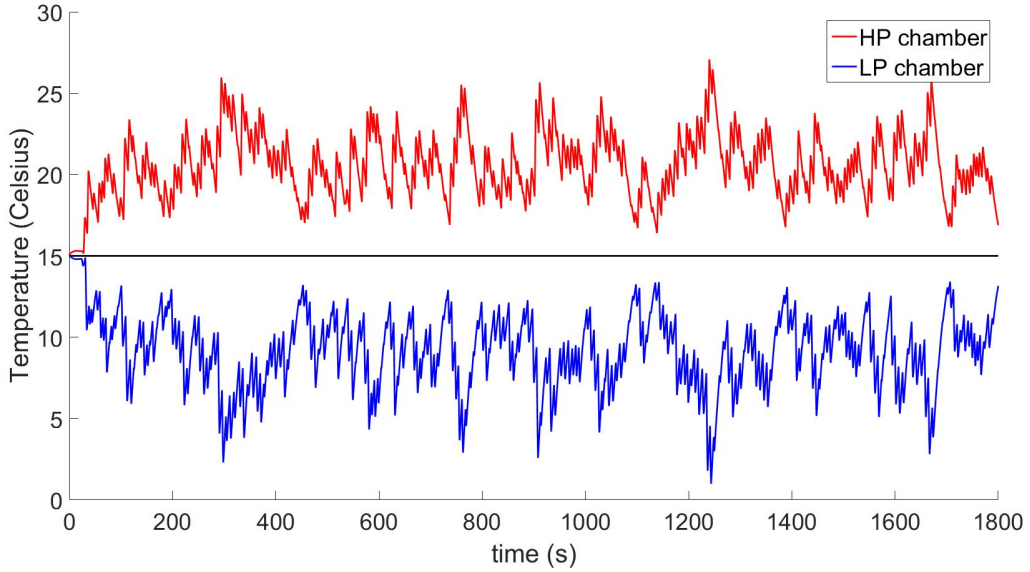

Figure 12: Air temperature in HP and LP chambers with isentropic model for sea state $\{H_s = 3\,\mathrm{m}\,;\, T_p = 9\,\mathrm{s}\}$

3.1.2. In the conventional OWC

In the case of the conventional OWC, a slight temperature increase in the OWC chamber is also observed. During the inhalation process, the viscous losses at the turbine result in an increase of specific internal energy in the OWC chamber. But unlike the Tupperwave device, the OWC chamber is open to the atmosphere whose temperature remains constant. This prevents large increase in temperatures. Figure 13 displays the temperature of the OWC chamber in the conventional OWC device in sea state $\{H_s = 3\,\mathrm{m}\,;\, T_p = 9\,\mathrm{s}\}$. The average temperature of the chamber towards the end of the simulation (represented by the black line) is 1.5°C higher than the initial temperature. In 5m high waves, the increase in temperature is of 3°C.

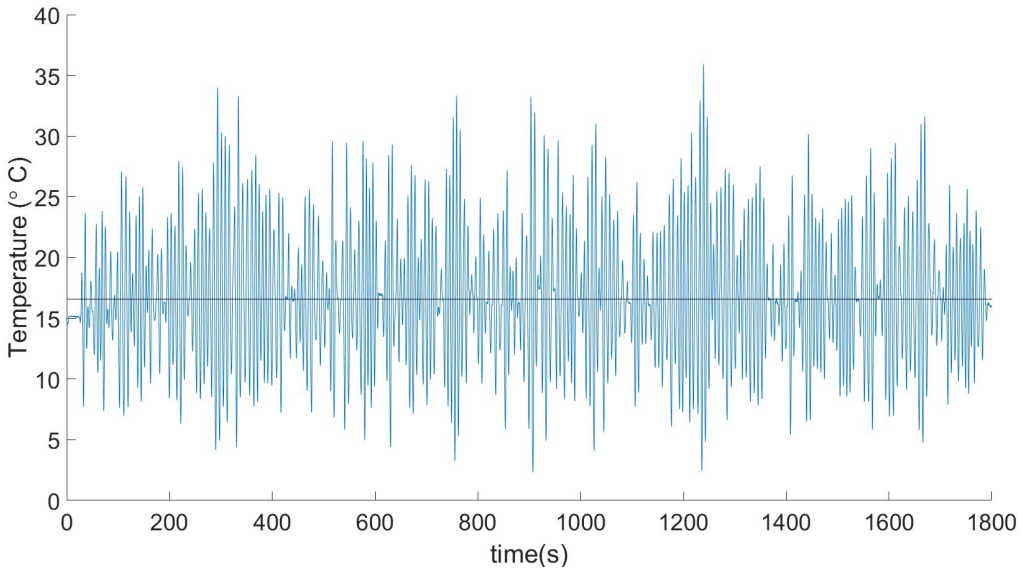

Figure 13: Air temperature of the OWC chamber of conventional OWC device for sea state $\{H_s = 3\,\mathrm{m}\,;\, T_p = 9\,\mathrm{s}\}$

3.2. Energy balance analysis

The review on wave-to-wire models of wave energy converters [27] distinguishes four main stages in the power conversion process of a wave energy converter: Absorption, transmission, generation and conditioning. In a conventional OWC, the power effectively absorbed from the waves P_{abs} is the power applied by internal water surface on the air contained in the OWC

chamber (absorption stage). This energy is briefly stored by the air contained in the OWC chamber under the form of internal energy and released, for the most part and with a delay, as power available to the turbine P_{avail}. This is the spring-like compressibility effect of the air [28]. We note that, if the process is assumed adiabatic and isentropic without any dissipative losses, the averaged values of the absorbed power and power available to the turbine over a sufficiently long time interval, must be equal $\overline{P_{avail}} = \overline{P_{abs}}$. This is not the case in the non-isentropic model of the conventional OWC developed in this study where the internal energy of the air is likely to change due to the heat transfer with the water column. Besides, in the case of the Tupperwave device, some energy is dissipated in the valves and the power available to the turbine is eventually lower than the power absorbed from the waves: $\overline{P_{avail}} < \overline{P_{abs}}$. Part of the power available to the turbine is then effectively converted by the turbine into mechanical power (transmission stage). The mechanical power is further converted into electrical power by the generator (generation stage). Finally, the raw electrical power created by the generator is adapted to be delivered into the grid by a power electronic converter (conditioning stage). In the present paper, the wave-to-wire models presented neglect the influence of the conditioning stage on the device efficiency. This simplification was shown in [29] to be perfectly reasonable in applications such as control parameters optimisation and power production assessment. Figure 14 displays a bar diagram of the average powers along the power conversion chain for the Tupperwave device. In the end, 57% of the absorbed power is converted in electrical power and the rest is disspated in the turbine, the valves and the generator.

In section 1.2.1, a general open thermodynamic system has been defined to derive the general equations relating mass, density, pressure and volume. These equations were then applied to each chamber of the Tupperwave device to build the numerical model. We now consider the thermodynamic system which refers to the total air contained in the Tupperwave device which is a closed system. According to the first law of thermodynamics, the change in the internal energy ΔU of a closed system is equal to the amount of heat supplied to the system, plus the amount of mechanical work W received by the system. The work received by the considered system is the work W_{abs} done by the internal water surface acting as a piston. The system also absorbs the heat Q_{rad} from the solar radiation. Within the system, part of the absorbed energy is dissipated in the turbine and valves W_{losses}.

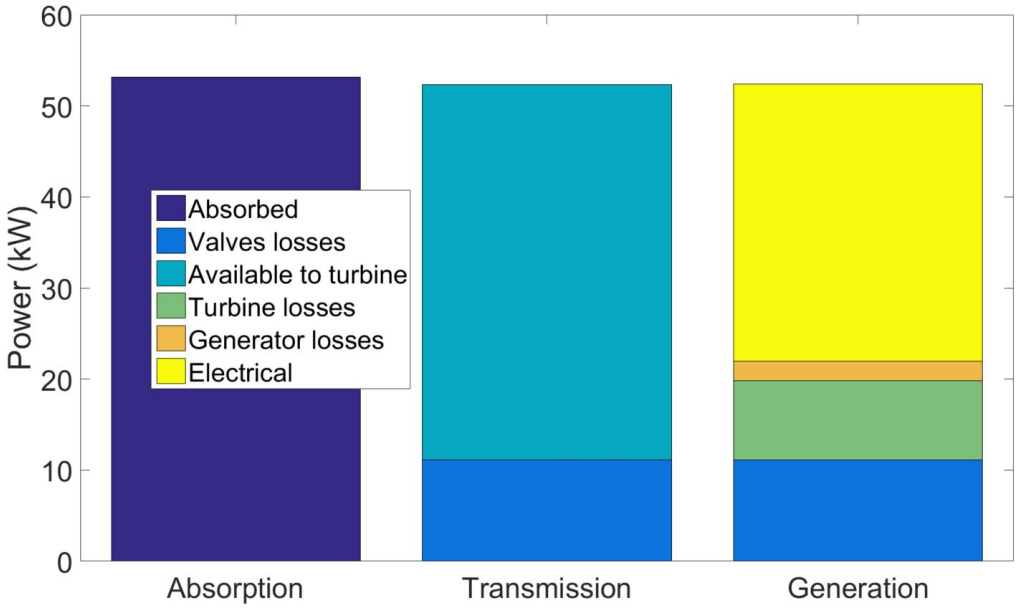

Figure 14: Diagram of average power along the conversion stages for sea state $\{H_s = 3\,\mathrm{m}\,;\, T_p = 9\,\mathrm{s}\}$ for the Tupperwave device with steel structure

The mechanical work done by the system is the work provided to the turbine W_{turb}. Finally, the heat Q_{out} is transferred to the environment via conduction and convection through the control surface. Figure 15 displays a schematic of the energy balance of the system. Exchanges are counted positive in the direction of the arrows. The energy balance is written as:

$$W_{abs} + Q_{rad} = \Delta U + W_{turb} + Q_{out} \tag{49}$$

Figure 16 and 17 displays the bar diagram illustrating the energy balance of the system after 30 minutes of simulation in sea state $\{H_s = 3\,\mathrm{m}\,;\, T_p = 9\,\mathrm{s}\}$ respectively with and without solar radiation. This verifies the conservation of energy in the numerical model. The solar radiation on the device has little impact on the output power since the average turbine output power is 2.2% higher with the high solar radiation than without solar radiation.

Once the air temperature in the device reaches a steady state, the average internal energy of the system does not vary any more over a time period in the order of 10 minutes. The heat Q_{out} transferred through the control surface is equal to the sum of the heat absorbed from the solar radiations Q_{rad} and the turbine and valves losses W_{losses}. Hence, the steady state conditions, over a

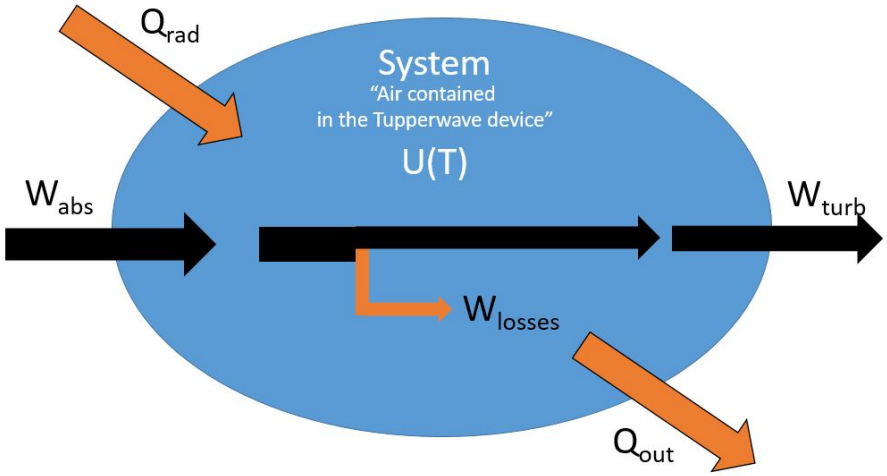

Figure 15: Energy balance schematic of the air contained in the Tupperwave device

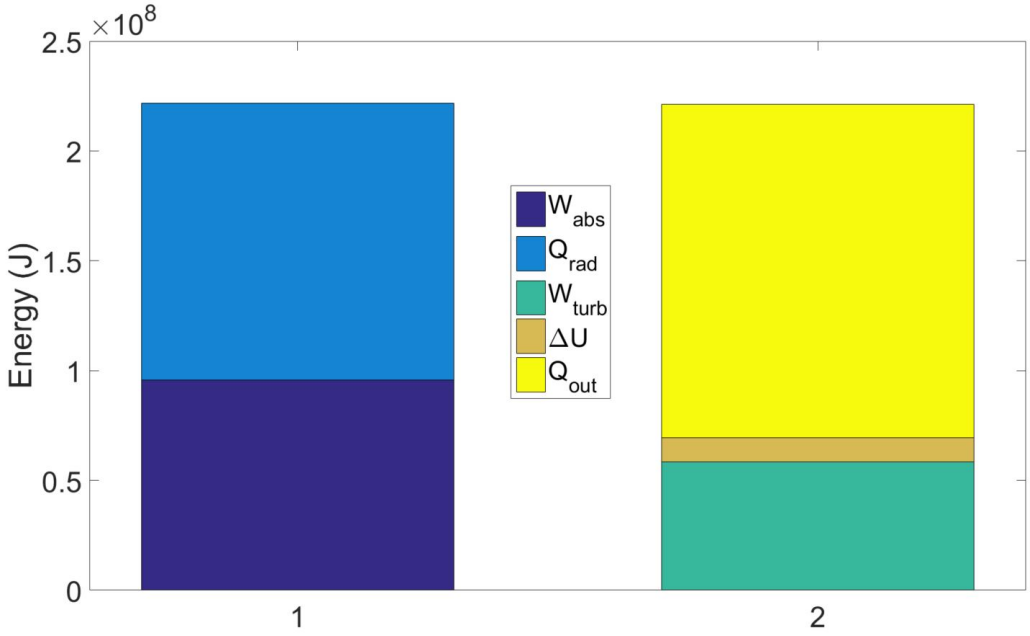

Figure 16: Energetic balance diagram of the air contained in the Tupperwave device with steel walls for sea state $\{H_s = 3\,\mathrm{m}\,; T_p = 9\,\mathrm{s}\}$ for a 30 minute simulation with solar irradiation $I_t = 1000\,\mathrm{W/m^2}$

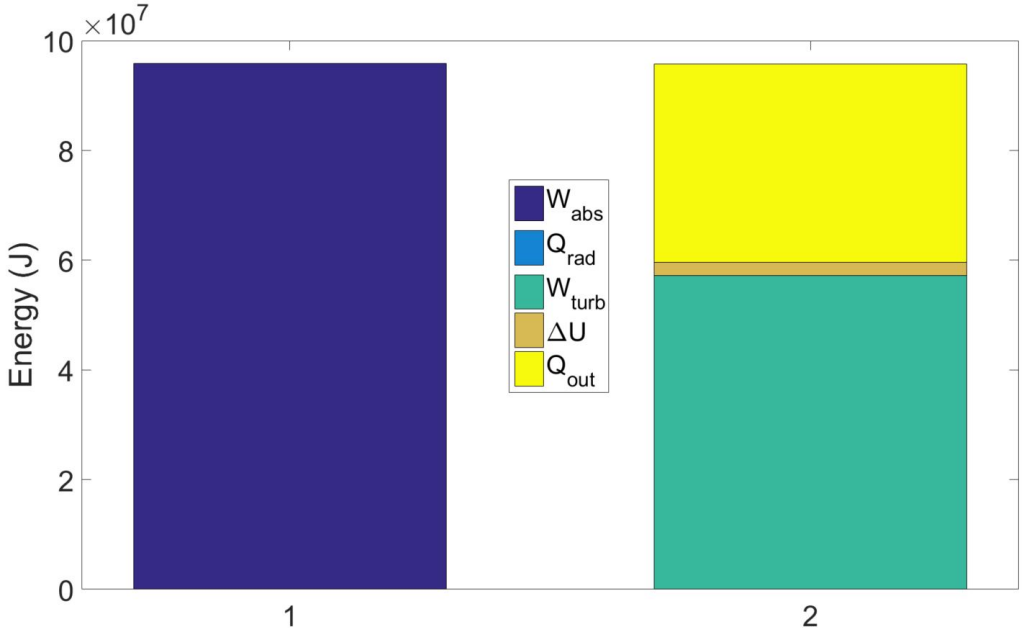

Figure 17: Energetic balance diagram of the air contained in the Tupperwave device with steel walls for sea state $\{H_s = 3\,\mathrm{m}\,;\, T_p = 9\,\mathrm{s}\}$ for a 30 minute simulation without solar irradiation

time period of about 10 minutes, are:

$$\begin{cases} \Delta U = 0 \\ Q_{rad} + W_{losses} = Q_{out} \end{cases} \tag{50}$$

We note that the turbine and valve losses do not depend on the material of the device walls. Thus, for the same solar radiation absorption, the heat transfer across the walls in steady state is independent from the wall material. Therefore, the steel device does not transfer more heat to the environment than the concrete device in steady state and their power output can be expected to be similar. This will be confirmed in the next section.

3.3. Isentropic / Non-isentropic comparison

In this section, the non-isentropic model results of the Tupperwave and corresponding conventional OWC devices presented in this paper, are compared to the model results using the linearised isentropic thermodynamic assumption, given in equation 14.

The devices were simulated in the wave climate of the EMEC wave energy test site. For the non-isentropic model, the yearly average global solar irradiance in the north of Scotland is $I_t = 115\,\mathrm{W/m^2}$ [30]. Table 3 displays the annual electrical power production of both devices in the EMEC wave climate, assessed with both non-isentropic model and linearised isentropic model.

Table 3: Annual electrical power production assessement with non-isentropic and isentropic models of the Tupperwave and conventional OWC devices

Annual production (MWh)	**Tupperwave**		**Conventional OWC**
	Concrete	**Steel**	
Non-isentropic	97.5	96.3	98.9
Isentropic linearised	97.6		99.9

The non-return valves are key components in the power conversion efficiency of the Tupperwave device. Depending on their characteristics (opening area and opening pressure), the Tupperwave device can either be more or less efficient than the conventional OWC. The influence of the valves characteristics was discussed in [6] and is not in the scope of this present paper. With the valves characteristics (opening area and pressure) used in this study, the Tupperwave device produces a similar amount of electrical energy as the conventional OWC.

The easier heat transfer to the environment through the walls of the steel device only reduces the electrical power output by 1-2% relative to the concrete device over a whole year on the EMEC test site.

Non-isentropic and isentropic models give very similar results as can be seen in figure 18 which displays the electrical power output time-series in a sea state. Over the whole year on the EMEC test site, the electrical power generation prediction obtained with both models differ by less than 1%. This shows that the isentropic linearized assumption provides satisfactory results for power production assessment in the case of the conventional OWC, as it was already shown in [7], and also in the case of the Tupperwave device.

4. Conclusion

In this paper, non-isentropic models of the Tupperwave device and corresponding conventional OWC were developed. The models account for the

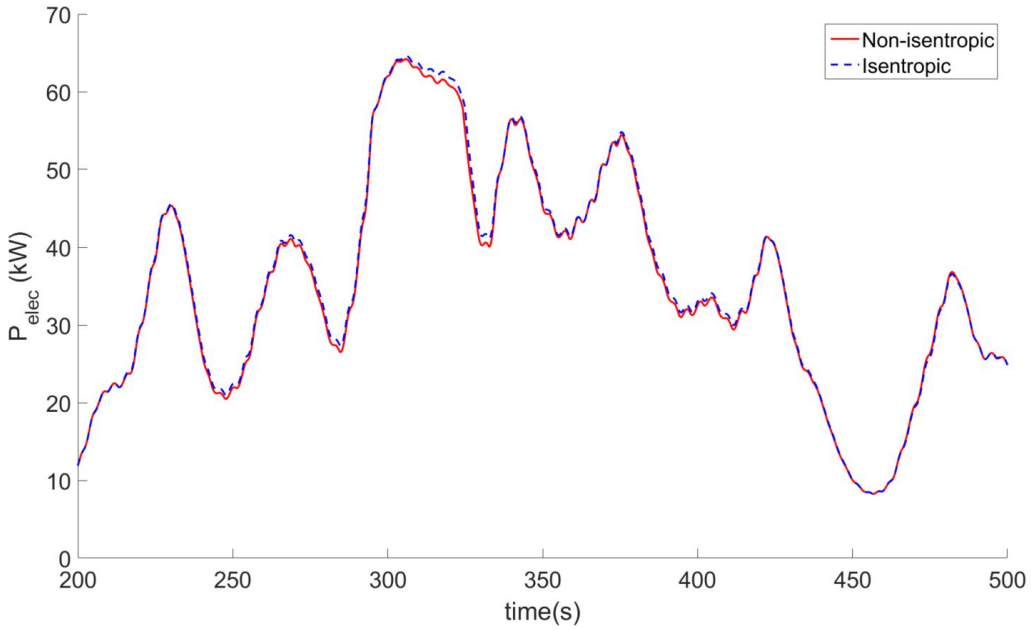

Figure 18: Time series of electrical output power of the Tupperwave device in sea state $\{H_s = 3\,\mathrm{m}\,;\, T_p = 9\,\mathrm{s}\}$ obtained with the non-isentropic model and isentropic model.

energy dissipation across the turbine and the valves, the heat transfers between the inner air and the environment, and the solar radiations on the device.

The results showed that the energy dissipation by viscous losses and the heat absorbed by the walls from solar radiations results in an increase in inner air temperature. The large surface area of the device outside walls allows sufficient heat transfer to the environment to limit the temperature increase to a certain threshold depending on the sea state, on the walls thermal conductivity, and on the level of solar irradiance. Eventually the internal air temperature does not reach any problematic value for the operation of the closed-circuit OWC device. This result demonstrate that the air temperature increase in a closed-circuit OWC device such as the Tupperwave device should not be considered as a barrier for the further development of this technology.

Whether steel or concrete walls are considered, the average temperature increase in the Tupperwave device does not exceed 16°C in very energetic sea states, even in very sunny days. For low thermal conductivity material

such as concrete, the heat transfer by convection and conduction through the walls is much longer to settle and the resistive heat transfer model used in this manuscript is not adapted to predict the temperatures increase caused by sudden increase of wave excitation force or solar radiation on the device. A more sophisticated heat transfer model would be necessary to correctly assess the transient state.

Similar temperature increase phenomenon was also observed in the corresponding conventional OWC device due to the viscous losses occurring in the turbine during the inhalation process. The temperature increase in the conventional OWC was however lower than in the Tupperwave device, since the air inhaled in every cycle is always at atmospheric temperature; the average temperature increase in the OWC chamber was limited to 3°C in very energetic sea states.

The results also showed that the solar radiation and the heat conductivity of the wall material have relatively small impact on the device electrical power output. The difference observed between high and low solar radiations, or between high and low heat conductivity of the walls, are in the order of 2%.

The more realistic non-isentropic models of the Tupperwave and conventional OWC devices were finally compared to the simpler models using linearised isentropic relationship between pressure and density within the chambers. The isentropic assumption was found to provide a satisfactory approximation of the power output for both open- and closed-circuit OWC devices. Realistic prediction of the temperatures in the devices can however only be achieved with the non-isentropic models.

Acknowledgement

The authors would like to acknowledge funding received through OCEANERA-NET European Network (OCN/00028).

References

[1] AFO. Falcão, JCC. Henriques, Oscillating-water-column wave energy converters and air turbines: A review, Renewable Energy 85 (2016) 1391–1424 (2016).

[2] A. Falcão, L. Gato, E. Nunes, A novel radial self-rectifying air turbine for use in wave energy converters. part 2. results from model testing, Renewable energy 53 (2013) 159–164 (2013).

[3] B. S. Lopes, LMC. Gato, AFO. Falcão, JCC. Henriques, Test results of a novel twin-rotor radial inflow self-rectifying air turbine for OWC wave energy converters, Energy 170 (2019) 869–879 (2019).

[4] A. Fleming, G. MacFarlane, S. Hunter, T. Denniss, Power performance prediction for a vented oscillating water column wave energy converter with a unidirectional air turbine power take-off, in: Proceedings of the 12th European Wave and Tidal Energy Conference, EWTEC, 2017 (2017).

[5] P. Benreguig, V. Pakrashi, J. Murphy, Assessment of primary energy conversion of a closed-circuit OWC wave energy converter, Energies 12 (10) (2019) 1962 (2019).

[6] P. Benreguig, J. Kelly, V. Pakrashi, J. Murphy, Wave-to-wire model development and validation for two owc type wave energy converters, Energies 12 (20) (2019) 3977 (2019).

[7] AFO. Falcão, PAP. Justino, OWC wave energy devices with air flow control, Ocean Engineering 26 (12) (1999) 1275–1295 (1999).

[8] W. Sheng, R. Alcorn, A. Lewis, On thermodynamics in the primary power conversion of oscillating water column wave energy converters, Journal of Renewable and Sustainable Energy 5 (2) (2013) 023105 (2013).

[9] C. Josset, A. Clément, A time-domain numerical simulator for oscillating water column wave power plants, Renewable energy 32 (8) (2007) 1379–1402 (2007).

[10] W. Sheng, R. Alcorn, A. Lewis, Assessment of primary energy conversions of oscillating water columns. i. hydrodynamic analysis, Journal of Renewable and Sustainable Energy 6 (5) (2014) 053113 (2014).

[11] C.-H. Lee, J. N. Newman, Wamit user manual, WAMIT, Inc (2006).

[12] R. Rajput, A textbook of engineering thermodynamics, Firewall Media, 2010 (2010).

[13] B. M. Marino, N. Muñoz, L. P. Thomas, Calculation of the external surface temperature of a multi-layer wall considering solar radiation effects, Energy and Buildings 174 (2018) 452–463 (2018).

[14] C. Hall, S. L. Dixon, Fluid mechanics and thermodynamics of turbomachinery, Butterworth-Heinemann, 2013 (2013).

[15] B. Lopes, Construction and testing of a double rotor self-rectifying air turbine model for wave energy recovery systems. language of reference: Portuguese., MSc thesis, Tecnico Lisboa, Portugal (2017).

[16] P. Benreguig, J. Murphy, W. Sheng, Model scale testing of the tupperwave device with comparison to a conventional OWC, in: Proceedings of the ASME 2018 37th International Conference on Ocean, Offshore and Arctic Engineering OMAE2018, Madrid, Spain, American Society of Mechanical Engineers (ASME), 2018 (2018).

[17] R. E. Sonntag, C. Borgnakke, G. J. Van Wylen, S. Van Wyk, Fundamentals of thermodynamics, Wiley New York, 1998 (1998).

[18] E. Tedeschi, M. Carraro, M. Molinas, P. Mattavelli, Effect of control strategies and power take-off efficiency on the power capture from sea waves, IEEE Transactions on Energy Conversion 26 (4) (2011) 1088–1098 (2011).

[19] W. Sheng, R. Alcorn, A. Lewis, A new method for radiation forces for floating platforms in waves, Ocean Engineering 105 (2015) 43–53 (2015).

[20] G. Duclos, A. H. Clément, G. Chatry, et al., Absorption of outgoing waves in a numerical wave tank using a self-adaptive boundary condition, International Journal of Offshore and Polar Engineering 11 (03) (2001).

[21] E. Dick, Fundamentals of turbomachines, Vol. 109, Springer, 2015 (2015).

[22] Guide A environmental design, The Chartered Institution of Building Services Engineers (CIBSE), London, available at: `https://www.cambeep.eng.cam.ac.uk/References/cibse` (accessed June 14, 2019) (2006).

[23] M. Bahrami, Forced convection heat transfer, Simon Fraser University SFU, British Columbia, Canada, available at: `https://www.sfu.ca/~mbahrami/ENSC%20388/Notes/Forced%20Convection.pdf` (accessed June 14, 2019) (2019).

[24] T. Namèche, J. Vassel, Thermal balance in temperate climate of aerated and natural lagoons; language of reference: French, Revue des sciences de l'eau/Journal of Water Science 12 (1) (1999) 65–91 (1999).

[25] L. Guo, L. Guo, L. Zhong, Y. Zhu, Thermal conductivity and heat transfer coefficient of concrete, Journal of Wuhan University of Technology-Mater. Sci. Ed. 26 (4) (2011) 791–796 (2011).

[26] M. J. Hancock, The 1-d heat equation, MIT OpenCourseWare, Massachusetts Institute of Technology, available at: https://ocw.mit.edu/courses/mathematics/18-303-linear-partial-differential-equations-fall-2006/lecture-notes/heateqni.pdf (accessed June 17, 2019) (2006).

[27] M. Penalba, J. V. Ringwood, A review of wave-to-wire models for wave energy converters, Energies 9 (7) (2016).

[28] AFO. Falcão, JCC. Henriques, The spring-like air compressibility effect in OWC wave energy converters: hydro-, thermo- and aerodynamic analyses, in: ASME 2018 37th International Conference on Ocean, Offshore and Arctic Engineering, 2018 (2018).

[29] M. Penalba, JV. Ringwood, A reduced wave-to-wire model for controller design and power assessment of wave energy converters, in: Advances in Renewable Energies Offshore: Proceedings of the 3rd International Conference on Renewable Energies Offshore (RENEW 2018), October 8-10, 2018, Lisbon, Portugal, CRC Press, 2018, p. 379 (2018).

[30] M. Suri, T. Huld, E. Dunlop, T. Cebecauer, Photovoltaic solar electricity potential in European countries, Institute for Environment and Sustainability, available at: http://re.jrc.ec.europa.eu/pvgis/download/PVGIS-EuropeSolarPotential.pdf (2006).